**Soils and Rocks**
*An International Journal of Geotechnical and Geoenvironmental Engineering*
www.soilsandrocks.com
ISSN 1980-9743
ISSN-e 2675-5475

# Mechanical behavior of zinc ore tailings over a broad range of confining stresses

Luciana Prado Leite Praça[1], Bruna Zakharia Hoch[1],
Hugo Carlos Scheuermann Filho[1], Fernando Schnaid[1], Lucas Festugato[1#]

**Article**

**Keywords**
Zinc mining tailings
Geomechanical behavior
High effective stress
Isotropic compression line
Critical state line
Particle breakage

**Abstract**

A proper evaluation of the mechanics of tailings is a crucial step toward the geotechnical analyses required throughout the project lifecycle of tailings storage facilities. In particular, an essential aspect of behavior is the stress level dependency of the stress-deformation constitutive relationships, which needs to be assessed when a new dam is raised or when a new deposition of tailings occurs. For that purpose, the present paper addresses the response of zinc tailings under triaxial compression tests with confinement pressures ranging from 20 kPa to 4000 kPa. Particle breakage was assessed by determining the grain size distribution in some specimens sheared at specific confining pressures. The results indicate the existence of multiple-strength envelopes in which the critical stress ratio ($M$) varied from 1.58 for the lowest confinement levels to 1.20 for the highest pressures. This was accompanied by a substantial increment in the acceptable content of the material, resulting from grain crushing occurring at higher pressures.

## 1. Introduction

Tailings are residues derived from ore beneficiation processes and are mainly composed of crushed rocks, fines, chemicals, and elevated amounts of water (Wang et al., 2014; Xiaolong et al., 2021). Then, tailings usually present an aqueous slurry form, facilitating their hydraulic disposal in large impoundments termed tailings dams (Vick, 2020). The upstream method, at which the raising dykes are founded above the deposited tailings, preponderates in low-risk seismic areas because of the short-term economic convenience (Du et al., 2019; Kossoff et al., 2014). Still, tailings are routinely saturated and loose, thus susceptible to flow and cyclic liquefaction. It is no coincidence that most incidents reported in tailings dams involved upstream heightened structures, with severe social and environmental consequences (Islam & Murakami, 2021; Lyu et al., 2019).

For this reason, an overall understanding of tailings behavior, particularly considering the boundary conditions encountered on field, is essential for the proper design and management of an upstream heightened tailings dam. In other words, obtaining reliable and representative parameters is necessary to describe the tailings' constitutive behavior within the dam adequately. Nevertheless, the mean stress at which the tailings are submitted is proportional to the dam's height, which usually increases when the reservoir's capacity augments. Fabric alterations associated with changes in the material's gradation and particle rearrangement may accompany this phenomenon, possibly leading to the stress dependency of the critical state friction angle ($\phi_c'$) (Consoli et al., 2023; Zhang & Luo, 2020).

Therefore, the present research intends to address this issue by investigating the behavior of zinc tailings under a broad range of effective confining pressures from triaxial compression testing. Specifically, 11 isotropically consolidated undrained triaxial compression tests (CIU) were carried out under confinements ranging from 20 to 4,000 kPa. The results were analyzed in the light of critical state soil mechanics, with particle breakage assessment for tests performed at higher stresses.

## 2. Experimental program

The experimental program was conducted in three parts. First, the zinc ore tailings were characterized physically, chemically, and mineralogically. Next, undrained triaxial tests were performed, and finally, the after-shearing particle size distribution was evaluated for specific effective confining pressure values.

[#]Corresponding author. E-mail address: lucas@ufrgs.br
[1]Universidade Federal do Rio Grande do Sul, Programa de Pós-graduação em Engenharia Civil, Porto Alegre, RS, Brasil.
Submitted on June 27, 2024; Final Acceptance on January 5, 2026; Discussion open until November 30, 2026.
Editor: Renato P. Cunha

https://doi.org/10.28927/SR.2026.005224

## 2.1 Materials

The zinc tailings were collected in a disturbed state from a dam in the Minas Gerais province in Southeast Brazil. The average water content ($w$) was about 132%, whereas the mean bulk unit weight lay around 13.1 kN/m$^3$. Table 1 summarizes the main physical characteristics of the material; Figure 1 presents its grain size distribution. The grain size distribution was determined through sedimentation following the ASTM D7928 normative (ASTM, 2021). The specific gravity and the Atterberg limits were assessed by ASTM D854 (ASTM, 2023) and ASTM D4318 (ASTM, 2017b) standards, respectively. According to the unified soil classification system (ASTM, 2017a) zinc tailings are classified as silty clay with sand (MH). Hlenka (2012) reported similar results regarding the grain size distribution (clayey fraction varying from 16.7% to 20.4%) but an elevated variation of the plastic index (25% to 54%). The latter is probably related to the chemical constituents in the zinc tailings, which may affect the analysis of a clastic and anthropic material using a technique employed for natural soils.

**Table 1.** Physical properties of the Zinc tailings.

| Physical properties | Zinc tailings | Test method |
|---|---|---|
| Liquid limit (%) | 68 | ASTM D4318 |
| Plastic limit (%) | 44 | |
| Plastic index (%) | 22 | |
| Specific gravity | 3.18 | ASTM D854 |
| Coarse Sand (2.00 mm < diameter < 4.75 mm) (%) | 0 | ASTM D7928 |
| Medium Sand (0.425 mm < diameter < 2.00 mm) (%) | 3.0 | |
| Fine Sand (0.075 mm < diameter < 0.425 mm) (%) | 12.0 | |
| Silt (0.002 < diameter < 0.075 mm) (%) | 69.0 | |
| Clay (diameter < 0.002 mm) (%) | 16.0 | |
| Effective diameter ($D_{10}$) (mm) | 0.0095 | |

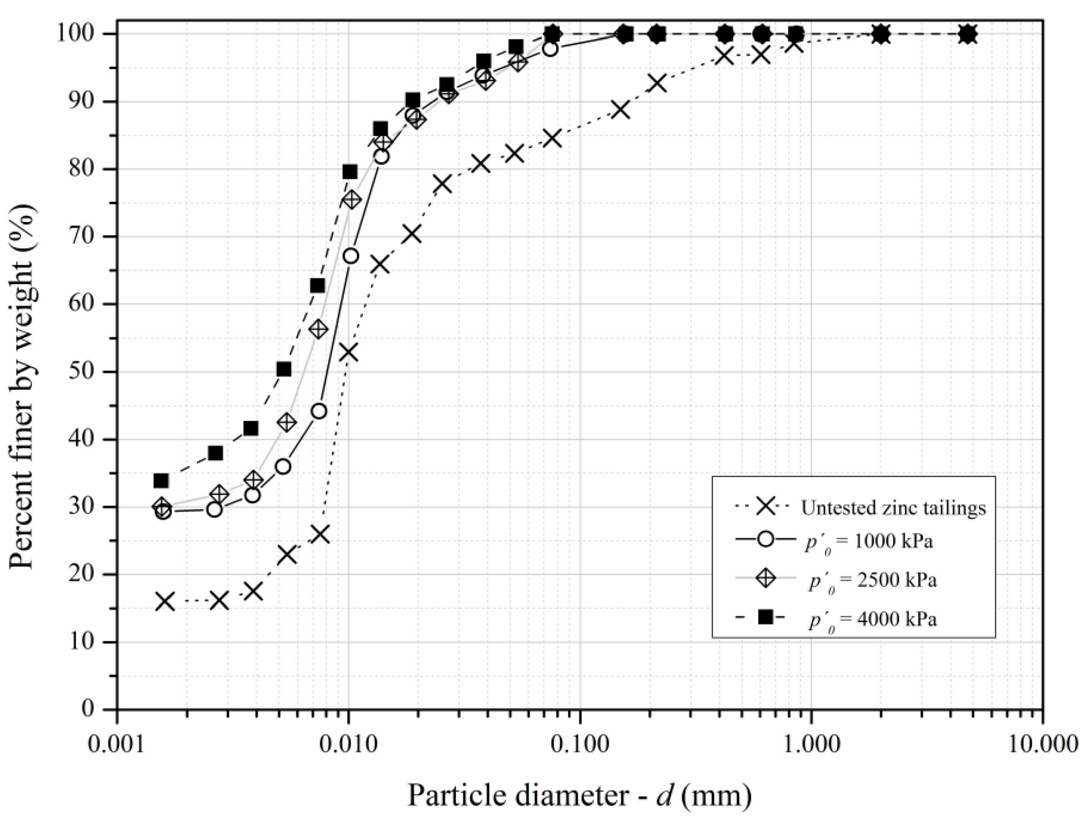


**Figure 1.** Granulometry of zinc tailings untested and after shearing at 1,000, 2,500 and 4,000 kPa.

Chemically, X-ray fluorescence tests (XRF) revealed that this residue is primarily composed of sulfur (S) (34.20%), iron (Fe) (28.08%), calcium (Ca) (15.83%), zinc (Zn) (10.92%), and lead (Pb) (5.96%). Mineralogically, X-ray diffraction tests (XRD) attested the presence of calcium sulfate hydrate ($CaSO_4.H_20$), zinc sulfide (ZnS), katoite ($Ca_3Al2O_6$), lead sulfate ($PbSO_4$), magnetite ($Fe_3O_4$), and lead oxide (PbO). The XRD pattern is presented in Figure 2. The presence of calcium sulfate brought difficulties to the Atterberg limits determination because it crystalizes at temperatures greater than 100°C. Hence, exothermic reactions occurred when the dried tailings were in contact with water due to the conversion of the crystallized sulfate to gypsite, calcium sulfate hydrate, or calcium sulfate hemihydrate. The conversion to the hemihydrate phase causes an unexpected hydration called apparent setting, leading to premature stiffening of the material, thus altering the workability of the zinc tailings. Mehta (1983) reported a similar trend. The samples collected directly from the dam were dried and tested without water addition to overcome the setting influence.

## 2.2 Methods

### 2.2.1 Specimens molding

Cylindrical specimens (50 mm in diameter and 100 mm in height) were individually molded for the triaxial tests using the moist tamping technique (David Suits et al., 2003). The molding process was initiated by weighing the previously dried zinc tailings (the drying occurred at 60°C to avoid undesirable reactions with the zinc tailings). Following this, distilled water was added (20% by dry weight of tailings) to the correct amount of tailings, and the material was mixed until it acquired a uniform consistency. Next, the humid mixture was carefully compacted in five layers of equal height directly into the latex membrane used for the triaxial test to the previously assigned void ratio. Five layers were used to ensure homogeneity regarding the density of the samples; the compaction slightly diminished in the upper layers to avoid the over-compaction of the lower layers. This membrane was positioned inside a cylindrical split mold with a vacuum pump. In an attempt to reproduce the on-field loose condition of the zinc tailings and expecting the existence of a unique isotropic compression line (ICL) which would be reached during the consolidation phase, the specimens were prepared with initial void ratio ($e_0$) ranging from 2.62 to 3.14. Nonetheless, on the one hand, the adopted molding technique may not be able to reproduce the fabric of the tailings as encountered on certain parts of the dam (Shaker & Elkady, 2015; Velten et al., 2022; Yimsiri & Soga, 2011), On the other hand, the effect of fabrics arising from distinct sample preparation methods is small at larger strain values, as demonstrated from previous work in iron ore tailings (Li & Coop, 2019) and gold tailings (Bedin et al., 2012; Chang et al., 2011; Fotovvat & Sadrekarimi, 2022; Li et al., 2018). Also, moist tamping can guarantee a more precise control of the molding void ratio.

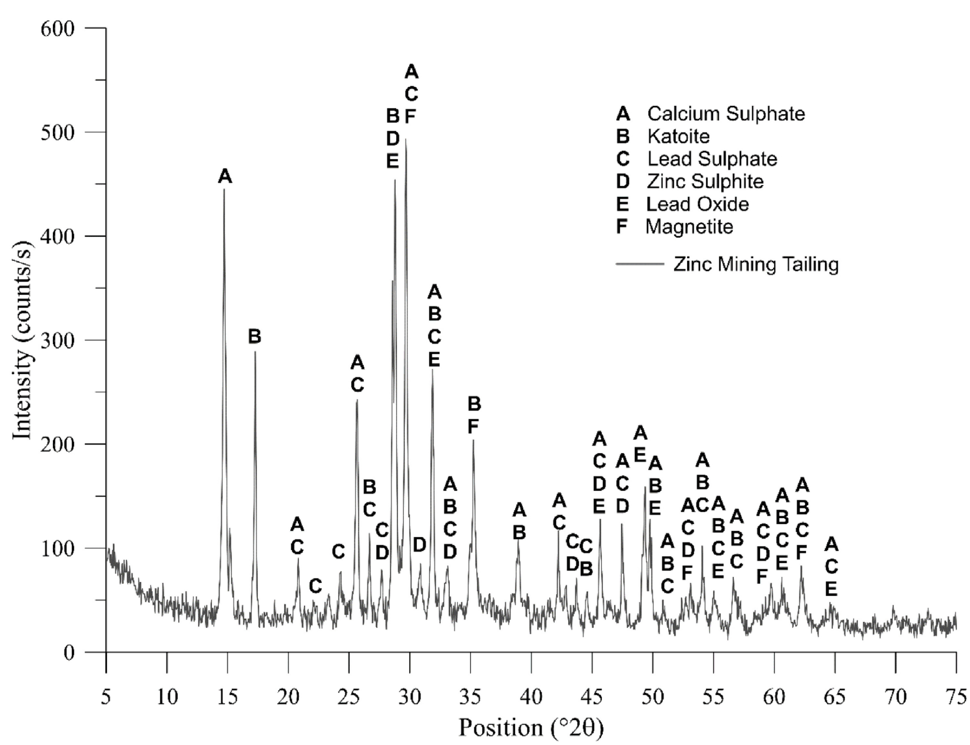


**Figure 2.** XRD pattern of the zinc ore tailings.

### 2.2.2 Triaxial tests

Eleven consolidated undrained triaxial compression tests were carried out using the procedures recommended by ASTM D4767 (ASTM, 2020). Initial effective confining pressures ($p'_0$) ranging from 20 kPa to 4,000 kPa (Table 2) were utilized. The testing specimens were fully saturated using a process that encompassed (i) percolation of carbon dioxide ($CO_2$), (ii) percolation of distilled water, and (iii) increments in backpressure until the attainment of a B-value greater than 0.95. During this last stage, the backpressure increased at an 8 kPa/min rate, but the mean effective stress ($p'$) was maintained at a constant value of 20 kPa. Such a rate is adequate to guarantee enough time for pressure equalization. A backpressure value of 400 kPa was sufficient to guarantee specimen saturation; once this process was accomplished, the consolidation began by augmenting the confining pressure at a continuous rate of 2 kPa/min up to the desired confinement value. Then, the testing sample was sheared at a displacement rate of 2 mm per hour, under undrained conditions, up to minimum axial deformations ($\varepsilon_a$) of 20%. The triaxial apparatus allowed axial and radial displacement assessment by internal and external systems. Internally, local strains were measured using Hall effect sensors, having a resolution lower than 1 μm (Clayton & Khatrush, 1986). Externally, an LVDT, with a resolution of around 10μm, measured the relative displacement between the triaxial chamber and the loading piston. Two computer-assigned digital pressure/volume controllers controlled the confinement pressure and backpressure.

## 3. Results and discussion

### 3.1 Stress-strain behavior

Table 2 summarizes the testing conditions of the eleven triaxial tests performed herein; Figure 3 presents the stress-strain response ($q$ x $\varepsilon_a$) and the pore water pressure variation ($u$ x $\varepsilon_a$) registered during the undrained shearing. Most of the tests presented a ductile response characterized by a rapid strength gain followed by stabilization. This was accompanied by a fast increment in pore water pressure ($u$) followed by a steady state, or even a slight decrement, up to the end of shearing. This indicates a contractive trend if the specimens were sheared under drained conditions. Test 01, sheared under the lowest confining pressure ($p'_0$ = 20 kPa), is an exception: it exhibited negative pore pressure variation, which would characterize a dilatative response in drained shearing. Those tendencies are corroborated by the normalized stress ($q/p'$ x $\varepsilon_a$) and pore water pressures ($u/p'$ x $\varepsilon_a$) results shown in Figure 4.

As for large deformations, a unique critical state stress ratio ($M$) has not been achieved for all tested specimens. This is noticeable in the normalized stress plots, at which $q/p'$ ranging from 0.8 to 1.8 suggested either a non-linearity of the critical state line (CSL) in the effective stress plane or that the critical state has not been reached for all the samples (Bedin et al., 2012). Figure 5 illustrates the after-shearing conditions of the zinc tailings specimens tested at higher confinement levels ($p'_0$ = 1000, 2500, and 4000 kPa), highlighting a substantial reduction in the height of the samples and the presence of inclined failure planes of around 75°. Thus, care was taken to correct the cross-section area (La Rochelle et al., 1988).

### 3.2 Stress-paths

Figure 6a shows the stress paths in the effective stress plane ($p'$:$q$) for all tested specimens; Figure 6b presents the test data considering the lower confinement levels ($p'_0 \leq$ 330kPa). Although the final conditions of each test have not produced a single strength envelope, an attempt to fit a unique stress-strength relationship to the results evolved to a critical state stress ratio ($M$) equal to 1.20, which corresponds to a critical state effective friction angle ($\phi'_{cs}$) of 30.2° (Figure 6a). Nonetheless, once the results relative to distinct ranges of initial confining pressures

**Table 2.** Summary of triaxial testing data.

| Test no. | Molding void ratio, $e_0$ | After consolidation void ratio, $e_{sh}$ | Initial mean effective stress, $p'_0$ (kPa) | Top deviatoric stress, $q_{max}$ (kPa) | Top excess pore pressure, $u_{max}$ (kPa) |
|---|---|---|---|---|---|
| 01 | 2.976 | 2.965 | 20 | 84.97 | 14.78 |
| 02 | 3.002 | 2.944 | 60 | 108.90 | 63.00 |
| 03 | 2.612 | 2.573 | 75 | 171.08 | 55.74 |
| 04 | 3.075 | 2.761 | 275 | 349.40 | 191.59 |
| 05 | 3.083 | 2.804 | 330 | 356.76 | 327.66 |
| 06 | 3.142 | 2.554 | 1000 | 950.10 | 574.37 |
| 07 | 3.042 | 2.306 | 2500 | 2426.64 | 2488.2 |
| 08 | 2.973 | 2.196 | 4000 | 3348.66 | 2926.45 |
| 09(1) | 2.699 | 2.679 | 1000 | 867.44 | 485.83 |
| 10(1) (2) | 2.686 | 2.539 | 1000 | 1001.18 | 535.15 |
| 11(1) | 2.784 | 2.696 | 2250 | 2088.77 | 750.39 |

(1)Tests carried out to maximum axial strain lower than 20%; (2)Test carried out with 2 unloading-reloading cycles.

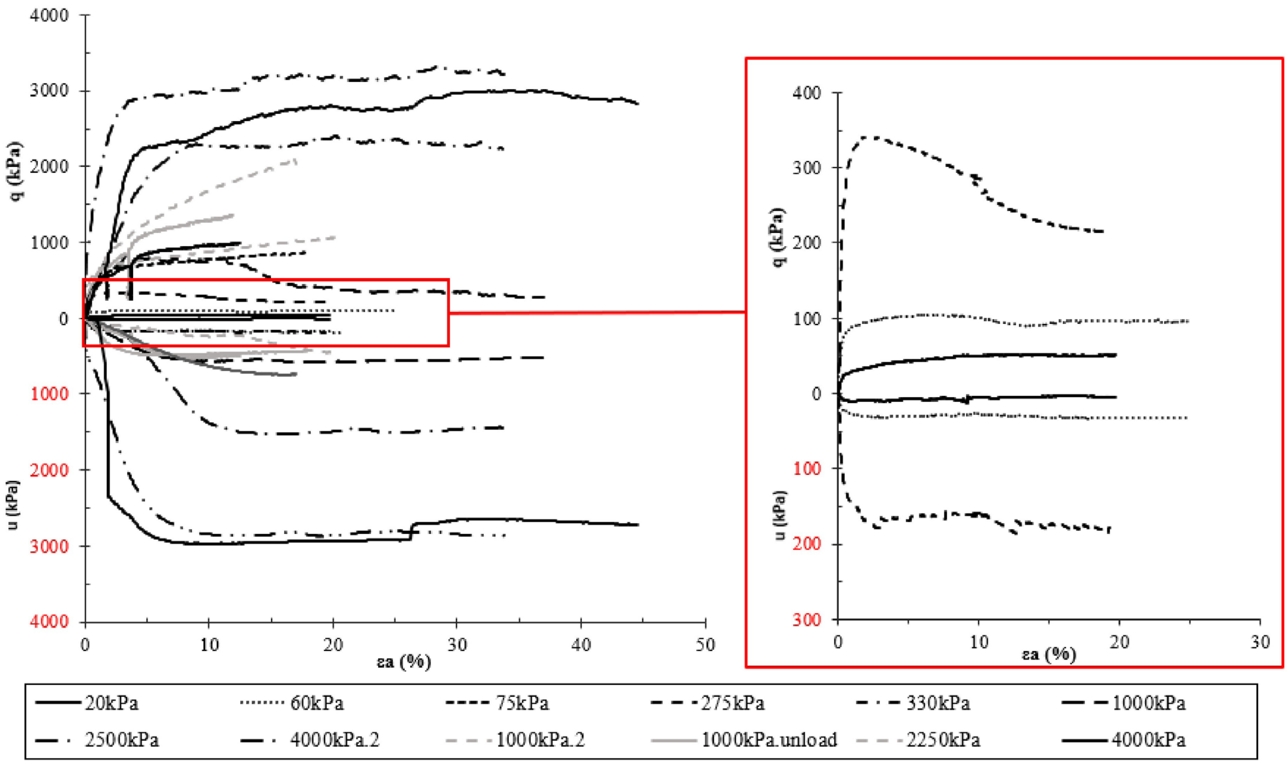


(a) (b)

**Figure 3.** Deviatoric stress and pore pressure against axial strain: (a) all results; (b) tests at confining stresses ≤ 400kPa (expanded scale).

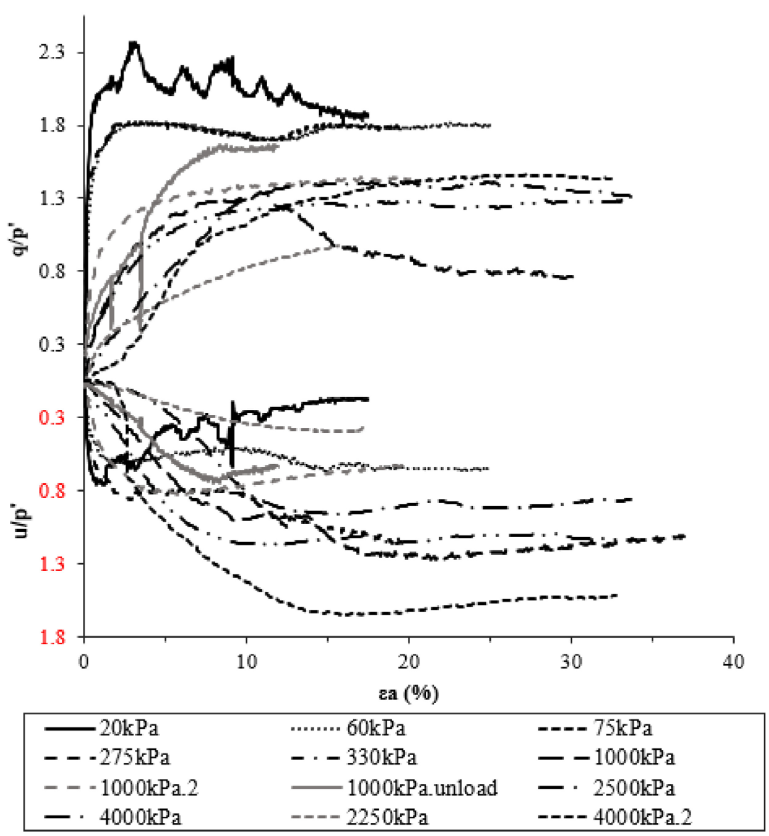


**Figure 4.** Normalized deviatoric stresses and pore water pressures against axial strain.

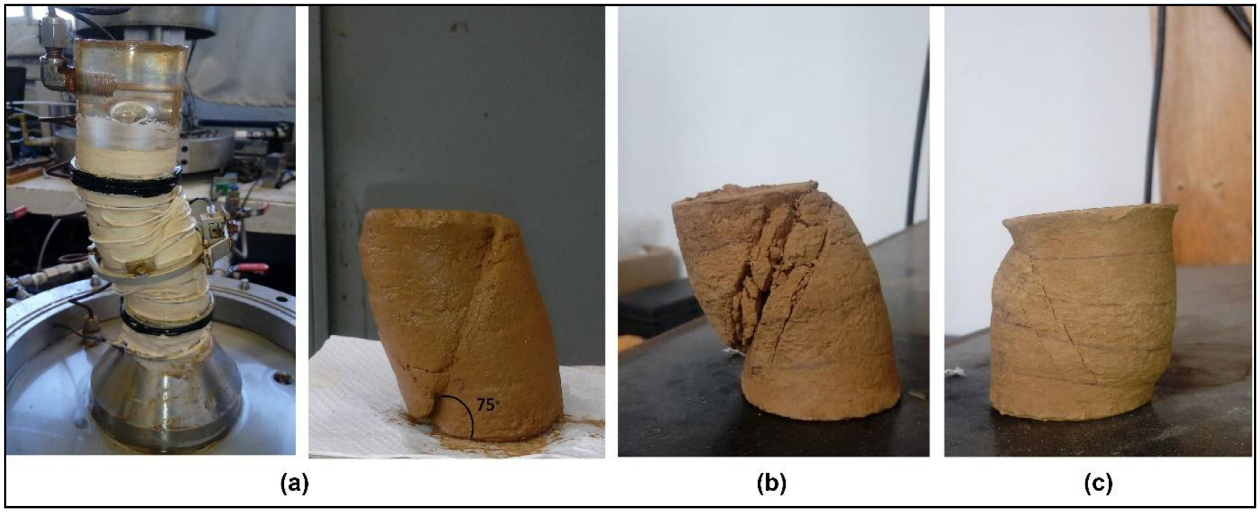


**Figure 5.** Specimens after shearing: (a) $p'$ = 1000 kPa; (b) $p'$ = 2500 kPa; (c) $p'$ = 4000 kPa.

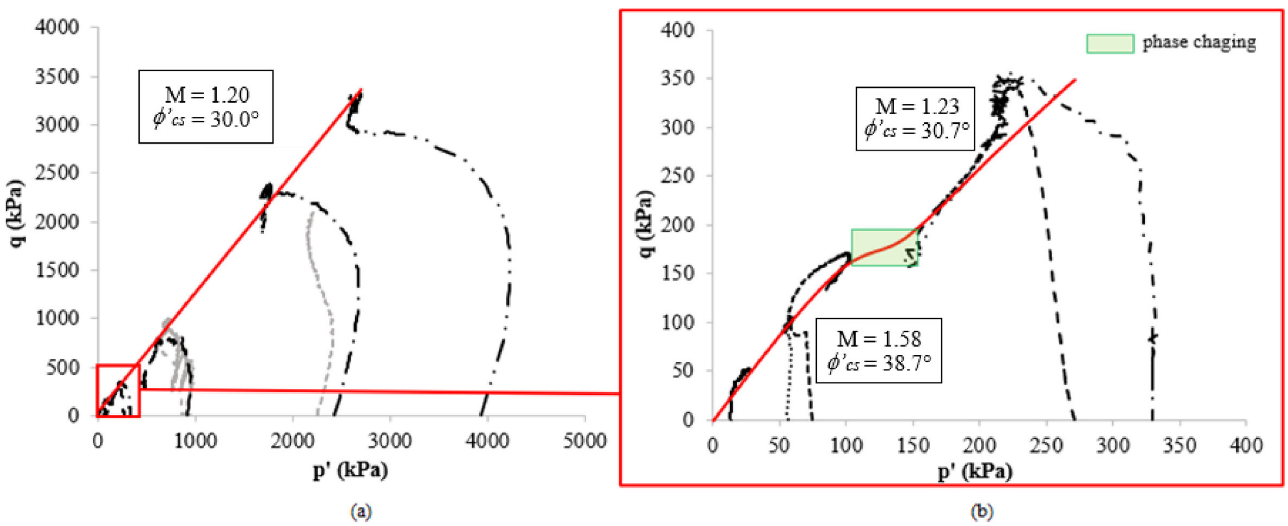


**Figure 6.** Stress paths of zinc tailings. (a) all results; (b) stress path at confining stresses ≤ 400kPa.

are independently analyzed (Figure 6b), different strength envelopes seem to coexist. The tests performed at the three lowest initial confining pressures ($p'_0 \leq$ 75kPa) have yielded a critical state stress ratio ($M$) of 1.58 ($\phi'_{cs}$ = 38.7°). A phase change appears to occur for specimens sheared at greater $p'_0$ values. This implied a decline of the $M$ value to 1.23 ($\phi'_{cs}$ = 30.7°), further decreasing to 1.20 when the highest confining pressures were applied (Figure 6a).

Figure 7 presents the stress paths of tests conducted at initial confining pressures of 1000 kPa but having distinct initial void ratios ($e_{sh}$) at the beginning of the shearing phase (tests no. 6, 9, and 10). In Test 10, two unloading/reloading phases were performed, as seen in Figure 7. All specimens presented initial positive pore water pressure generation (↑$u$). Still, phase change occurred at the end of tests no. 9 and 10, with the decay in the pore water pressure.

3.3 Particle breakage analysis

The extension of particle breakage occurring during shearing was assessed by evaluating the after-shearing particle size distribution (ASTM, 2021) of some of the zinc tailings ($p'_0$ = 1,000 kPa, 2,500 kPa, and 4,000 kPa). These results are depicted in Figure 1 and highlight the direct proportion between the confining level and the amount of particle breakage: the material got finer when sheared under higher $p'_0$ values. Table 3 quantifies such phenomenon by presenting representative diameters considering each grain size distribution and two particle breakage indexes: the relative breakage – $B_r$ (Hardin, 1985) and the particle breakage factor – $B_F$ (Nakata et al., 1999). The first is the ratio between the total amount of crushing that occurred during the test ($B_t$) and the breakage potential ($B_p$) of the

**Table 3.** Particle breakage parameters.

| Parameter | Untested | $p'_0$ = 1,000kPa | $p'_0$ = 2,500kPa | $p'_0$ = 4,000kPa |
|---|---|---|---|---|
| $D_{90}$ (mm) | 0.150 | 0.0382 | 0.0192 | 0.0186 |
| $D_{60}$ (mm) | 0.0101 | 0.0075 | 0.0075 | 0.0052 |
| $D_{50}$ (mm) | 0.0076 | 0.0075 | 0.0054 | 0.0037 |
| $D_{30}$ (mm) | 0.0076 | 0.0054 | 0.0038 | 0.0015 |
| $B_p$ | 4.60 | - | - | - |
| $B_t$ | - | 5.45 | 5.62 | 5.82 |
| $B_r$ | - | 1.18 | 1.22 | 1.27 |
| $B_F$ | - | 0.13 | 0.14 | 0.18 |

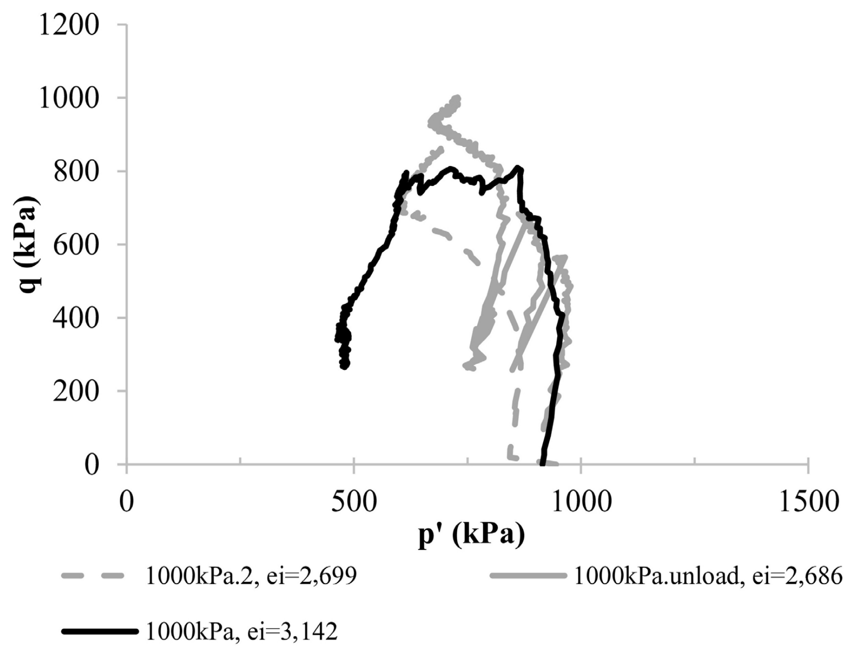


**Figure 7.** Stress paths of tests no. 6, 9, and 10, sheared at 1000 kPa.

untested material; the latter is simply the difference between the amount of the finer particles after testing in comparison to the original content of finer particles.

In brief, a substantial change is perceived between the gradation of the untested and tested (after-shearing) materials. Also, a slight distinction occurs amongst the grain size distribution of the sheared specimens ($p_0$' = 1000, 2500, and 4000 kPa). This agrees with the particle breakage parameters summarized in Table 3 and is considered strong evidence to explain the observed stress-strain behavior that ended up in multiple-strength envelopes (Bandini & Coop, 2011; Chang & Deng, 2020; Consoli et al., 2023).

### 3.4 Critical state

Figure 8 illustrates the isotropic compression paths and the shearing paths in the volumetric plane ($v$ - log $p'$) utilized for defining a unique isotropic compression line (ICL) and a single critical state line (CSL). Regardless of the initial specific volume ($v$), the specimens are directed towards the same line (i.e., the ICL) as the consolidation progresses. Moreover, an initially curved CSL, tending to linearity, seems to exist when considering the end-of-testing points. The marked curvature is probably related to fabric alterations owing to shearing. Such a shape indicates changes in the susceptibility to liquefaction with increased mean effective stress (Carrera et al., 2011; Li et al., 2018). That is, loose specimens (wet-side of the CSL) are more susceptible to liquefaction at lower stress levels (i.e., flatter portion of the CSL). A bilinear fit attempt, of the form of relationship of Equation 1, was proposed: the initial flatter part of the curve, up to a mean effective stress of around 100 kPa, has resulted in a CSL having a slope ($\lambda$) of 0.01 and an intercept ($\Gamma$) of 3.98, whereas the inclined portion yielded a CSL with $\lambda$ equals to 0.21 and a $\Gamma$ of 4.83.

$$\upsilon = \Gamma - \lambda \ln p' \tag{1}$$

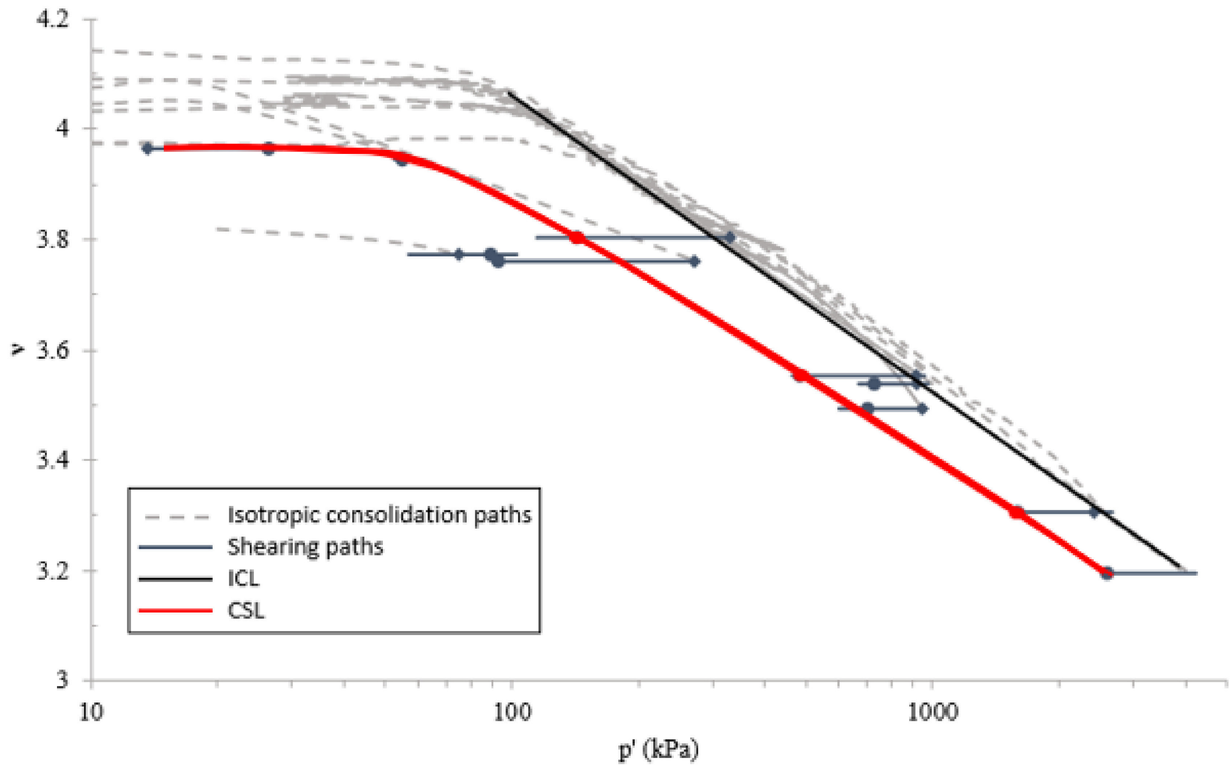


**Figure 8.** ICL and CSL in the volumetric plane.

## 4. Conclusions

The present study aimed to evaluate the mechanical response of zinc ore tailings over a broad range of confining pressures and investigate the material's gradation after shearing in triaxial compression. Conclusions drawn from this set of experimental results are:

- The material presented multiple strength envelopes, resulting in critical stress ratios (*M*) depending on the stress level. Higher *M* values were encountered for lower confining pressure levels in triaxial tests.
- The extension of particle breakage was proportional to the applied stress level, the amount of breakage was small as demonstrated by the particle breakage indexes. This has led to fabric alterations, which might have altered the material's stress-strain response.
- The shearing data of the zinc ore tailings resulted in a curved CSL that was initially flat for a mean effective pressure (*p'*) of up to 100 kPa. Such line configuration leads to liquefaction susceptibility changes when varying *p'*.

## Acknowledgements

Authors would like to acknowledge the Brazilian Research Council CNPq for funding this research (grants # 402572/2021-1 and # 307286/2022-3).

## Declaration of interest

The authors have no conflicts of interest to declare. All co-authors have observed and affirmed the contents of the paper and there is no financial interest to report.

## Authors' contributions

Luciana Prado Leite Praça: conceptualization, investigation, methodology, writing – original. Bruna Zakharia Hoch: investigation, methodology. Hugo Carlos Scheuermann Filho: formal analysis, writing – review & editing. Fernando Schnaid: visualization, writing – review & editing. Lucas Festugato: conceptualization, data curation, formal analysis, supervision, writing – review & editing.

## Data availability

The datasets generated analyzed during the current study are available from the corresponding author upon request.

## Declaration of use of generative artificial intelligence

This work was prepared without the assistance of any generative artificial intelligence (GenAI) tools or services. All aspects of the manuscript were developed solely by the authors, who take full responsibility for the content of this publication.

## List of symbols and abbreviations

| | |
|---|---|
| $e$ | void ratio |
| $e_0$ | void ratio prior to consolidation phase |
| $e_{sh}$ | void ratio prior to shearing phase |
| $p'$ | mean effective stress |
| $p'_0$ | mean effective stress the sample sheared from. |
| $q$ | deviatoric stress ($\sigma_1$ - $\sigma_3$) |
| $u$ | pore water pressure |
| $wt$ | weight percentage |
| $B_F$ | particle breakage factor |
| $B_p$ | breakage potential |
| $B_r$ | relative breakage |
| $B_t$ | total breakage |
| CSL | critical state line |
| CU | consolidated undrained |
| $D_n$ | "$n$%" of cumulate mass |
| ICL | isotropic compression line |
| $M$ | critical state stress ratio |
| $R^2$ | coefficient of determination |
| XRD | X-ray diffraction |
| XRF | X-ray fluorescence |
| $\lambda$ | slope of the CSL on the $\upsilon - \log p'$ plane |
| $\sigma_1$, $\sigma_3$ | principal stresses |
| $\upsilon$ | specific volume = 1 + $e$ |
| $\Gamma$ CSL | void ratio that corresponds to a mean effective stress of 1 kPa. |
| $\phi'$ | effective stress friction angle |
| $\phi_{cs}'$ | critical state friction angle |

## References

ASTM D2487. (2017a). *Practice for classification of soils for engineering purposes (unified soil classification system)*. ASTM International, West Conshohocken, PA. https://doi.org/10.1520/D2487-17E01.

ASTM D4318. (2017b). *Test methods for liquid limit, plastic limit, and plasticity index of soils*. ASTM International, West Conshohocken, PA. https://doi.org/10.1520/D4318-17E01.

ASTM D4767. (2020). *Test method for consolidated undrained triaxial compression test for cohesive soils*. ASTM International, West Conshohocken, PA. https://doi.org/10.1520/D4767-11R20.

ASTM D7928. (2021). *Test method for particle-size distribution (gradation) of fine-grained soils using the sedimentation (hydrometer) analysis*. ASTM International, West Conshohocken, PA. https://doi.org/10.1520/D7928-21E01.

ASTM D854. (2023). *Test methods for specific gravity of soil solids by water pycnometer*. ASTM International, West Conshohocken, PA. https://doi.org/10.1520/D0854-14.

Bandini, V., & Coop, M.R. (2011). The influence of particle breakage on the location of the critical state line of sands. *Soil and Foundation*, *51*(4), 591-600. https://doi.org/10.3208/sandf.51.591.

Bedin, J., Schnaid, F., Da Fonseca, A.V., & Costa Filho, L.D.M. (2012). Gold tailings liquefaction under critical state soil mechanics. *Geotechnique*, *62*(3), 263-267. https://doi.org/10.1680/geot.10.P.037.

Carrera, A., Coop, M., & Lancellotta, R. (2011). Influence of grading on the mechanical behaviour of Stava tailings. *Geotechnique*, *61*(11), 935-946. https://doi.org/10.1680/geot.9.P.009.

Chang, C.S., & Deng, Y. (2020). Modeling for critical state line of granular soil with evolution of grain size distribution due to particle breakage. *Geoscience Frontiers*, *11*(2), 473-486. https://doi.org/10.1016/j.gsf.2019.06.008.

Chang, N., Heymann, G., & Clayton, C. (2011). The effect of fabric on the behaviour of gold tailings. *Geotechnique*, *61*(3), 187-197. https://doi.org/10.1680/geot.9.P.066.

Clayton, C.R.I., & Khatrush, S.A. (1986). A new device for measuring local axial strains on triaxial specimens. *Geotechnique*, *36*(4), 593-597. https://doi.org/10.1680/geot.1986.36.4.593.

Consoli, N.C., Azambuja Carvalho, J.V.D., Wagner, A.C., Scheuermann Filho, H.C., Carvalho, I., Cacciari, P.P., & Sousa Silva, J.P.D. (2023). Determination of critical state line (CSL) for silty-sandy iron ore tailings subjected to low-high confining pressures. *Journal of Rock Mechanics and Geotechnical Engineering*, *16*(5), 1684-1695. https://doi.org/10.1016/j.jrmge.2023.06.014.

David Suits, L., Sheahan, T., Frost, J., & Park, J.-Y. (2003). A critical assessment of the moist tamping technique. *Geotechnical Testing Journal*, *26*(1), 9850. https://doi.org/10.1520/GTJ11108J.

Du, Y.Q., Xie, B., Mullarney, B., & Zhang, C. (2019). Deposition of fine tailing particles and profile zoning of tailings dams. *Soil Mechanics and Foundation Engineering*, *56*(5), 359-365. https://doi.org/10.1007/s11204-019-09615-5.

Fotovvat, A., & Sadrekarimi, A. (2022). Instability of a gold mine tailings subjected to different stress paths. *Journal of Geotechnical and Geoenvironmental Engineering*, *148*(5), 04022020. https://doi.org/10.1061/(ASCE)GT.1943-5606.0002780.

Hardin, B.O. (1985). Crushing of soil particles. *Journal of Geotechnical Engineering*, *111*(10), 1177-1192. https://doi.org/10.1061/(ASCE)0733-9410(1985)111:10(1177).

Hlenka, L. (2012). *Estudo dos efeitos da velocidade de carregamento na estimativa de parâmetros geotécnicos em resíduos de mineração de zinco* [Master's dissertation]. Universidade Federal do Rio Grande do Sul. Retrieved in June 27, 2024, from http://hdl.handle.net/10183/79806

Islam, K., & Murakami, S. (2021). Global-scale impact analysis of mine tailings dam failures: 1915–2020. *Global Environmental Change*, *70*, 102361. https://doi.org/10.1016/j.gloenvcha.2021.102361.

Kossoff, D., Dubbin, W.E., Alfredsson, M., Edwards, S.J., Macklin, M.G., & Hudson-Edwards, K.A. (2014). Mine tailings dams: Characteristics, failure, environmental impacts, and remediation. *Applied Geochemistry*, *51*, 229-245. https://doi.org/10.1016/j.apgeochem.2014.09.010.

La Rochelle, P., Leroueil, S., Trak, B., Blais-Leroux, L., & Tavenas, F. (1988). Observational approach to membrane and area corrections in triaxial tests. In R. Donaghe, R. Chaney, & M. Silver (Orgs.), *Advanced triaxial testing of soil and rock* (pp. 715-717). ASTM International. https://doi.org/10.1520/STP29110S.

Li, W., & Coop, M.R. (2019). Mechanical behaviour of Panzhihua iron tailings. *Canadian Geotechnical Journal*, *56*(3), 420-435. https://doi.org/10.1139/cgj-2018-0032.

Li, W., Coop, M.R., Senetakis, K., & Schnaid, F. (2018). The mechanics of a silt-sized gold tailing. *Engineering Geology*, *241*, 97-108. https://doi.org/10.1016/j.enggeo.2018.05.014.

Lyu, Z., Chai, J., Xu, Z., Qin, Y., & Cao, J. (2019). A comprehensive review on reasons for tailings dam failures based on case history. *Advances in Civil Engineering*, *2019*(1), 4159306. https://doi.org/10.1155/2019/4159306.

Mehta, P.K. (1983). Mechanism of sulfate attack on Portland Cement – Another look. *Cement and Concrete Research*, 13(3), 401-406. https://doi.org/10.1016/0008-8846(83)90040-6.

Nakata, A.F.L., Hyde, M., Hyodo, H., & Murata. (1999). A probabilistic approach to sand particle crushing in the triaxial test. *Geotechnique*, *49*(5), 567-583. https://doi.org/10.1680/geot.1999.49.5.567.

Shaker, A.A., & Elkady, T.Y. (2015). Hydraulic performance of sand–clay mixtures: soil fabric perspective. *Géotechnique Letters*, *5*(3), 198-204. https://doi.org/10.1680/jgele.15.00070.

Velten, R.Z., Consoli, N.C., Filho, H.C.S., Wagner, A.C., Schnaid, F., & Da Costa, J.P.R. (2022). Influence of grading and fabric arising from the initial compaction on the geomechanical characterisation of compacted copper tailings. *Geotechnique*, *74*(5), 461-472. https://doi.org/10.1680/jgeot.22.00087.

Vick, S.G. (2020). *Planning, design, and analysis of tailings dams*. Vancouver: BiTech Publishers. https://doi.org/10.14288/1.0394902.

Wang, C., Harbottle, D., Liu, Q., & Xu, Z. (2014). Current state of fine mineral tailings treatment: A critical review on theory and practice. *Minerals Engineering*, 58, 113-131. https://doi.org/10.1016/j.mineng.2014.01.018.

Xiaolong, Z., Shiyu, Z., Hui, L., & Yingliang, Z. (2021). Disposal of mine tailings via geopolymerization. *Journal of Cleaner Production*, 284, 124756. https://doi.org/10.1016/j.jclepro.2020.124756.

Yimsiri, S., & Soga, K. (2011). Effects of soil fabric on behaviors of granular soils: microscopic modeling. *Computers and Geotechnics*, *38*(7), 861-874. https://doi.org/10.1016/j.compgeo.2011.06.006.

Zhang, J., & Luo, M. (2020). Dilatancy and critical state of calcareous sand incorporating particle breakage. *International Journal of Geomechanics*, *20*(4), 04020030. https://doi.org/10.1061/(ASCE)GM.1943-5622.0001637.